Energy & Environmental Science

ROYAL SOCIETY OF CHEMISTRY

PAPER

View Article Online
View Journal | View Issue

Cite this: *Energy Environ. Sci.*, 2023, **16**, 4054

An immiscible phase-separation electrolyte and interface ion transfer electrochemistry enable zinc/lithium hybrid batteries with a 3.5 V-class operating voltage†

Ao Chen,[a] Yaqin Zhang,[a] Qing Li,[a] Guojing Liang,[a] Shuo Yang,[a] Zhaodong Huang,[b] Qi Yang,[b] Hong Hu,[a] Xinliang Li,[a] Ze Chen,[a] Jun Fan *[a] and Chunyi Zhi *[abcde]

The low-cost and high safety of zinc batteries have attracted tremendous attention in recent years. However, with conventional electrolytes, the operating voltages of zinc batteries are normally below 2 V. Hybrid batteries represented by commercial zinc–nickel batteries (zinc–proton hybrid batteries) employ H^+ as the charge carrier to obtain a high operating voltage and electrochemical performance. Nevertheless, the preparation of other alkaline zinc-based hybrid batteries with high electrochemical performance is difficult to achieve due to the narrow cathodic window and incompatibility of cathode materials with the alkaline electrolyte. Herein, we develop a unique phase-separation electrolyte (PSE) consisting of a completely immiscible aqueous phase and an oil phase. The alkaline aqueous electrolyte can take advantage of the low electrode potential of the zinc anode. The interface ion transfer electrochemistry in the PSE can further boost the operating voltage by ~0.35 V. Accordingly, our developed zinc/lithium hybrid batteries deliver an unprecedented average operating voltage of 3.41 V and a high energy density of 362.4 W h $kg_{anode+cathode}^{-1}$ (N/P is assumed to be 1), approaching the voltage of lithium-ion batteries. More interestingly, the liquid–liquid interface in the PSE can entirely intercept the propagation of zinc dendrites, benefiting from the completely blocked diffusion of Zn^{2+} into the oil phase. Zinc/lithium hybrid batteries with $LiMn_2O_4$ cathodes deliver an excellent cycle performance over 600 cycles with a 99.6% coulombic efficiency. To further demonstrate practicality, we fabricated a full cell with a commercial-level cathode mass loading of 18.3 mg cm^{-2}, achieving a zinc-based battery with a high voltage of 2.56 V and a high areal capacity of 2.14 mA h cm^{-2}.

Received 1st May 2023,
Accepted 26th July 2023

DOI: 10.1039/d3ee01362f

rsc.li/ees

Broader context

Limited by the electrochemical stability window (ESW) of conventional single aqueous electrolytes and cathode materials, the average operating voltage of zinc batteries is below 2 V. Hybrid batteries with flexible operability can deliver superior electrochemical performance compared to the traditional battery systems. Herein, we initiate a novel phase-separation electrolyte (PSE) with an ESW of 4.6 V, enabling the high voltage cathode materials to be used in zinc-based batteries. The alkaline zinc/lithium hybrid batteries employing lithium ions as the charge carrier achieved an unprecedented average operating voltage of 3.41 V. Interface ion transfer electrochemistry was found to increase the operating voltage by an additional ~0.35 V in the PSE. The investigation of employing unconventional electrolytes in zinc-based batteries provides a new pathway to develop battery systems with high electrochemical performances.

[a] *Department of Materials Science and Engineering, City University of Hong Kong, 83 Tat Chee Avenue, Kowloon, Hong Kong, China. E-mail: junfan@cityu.edu.hk, cy.zhi@cityu.edu.hk*
[b] *Hong Kong Center for Cerebro-Cardiovascular Health Engineering (COCHE), Shatin, NT, HKSAR, China*
[c] *Centre for Advanced Nuclear Safety and Sustainable Development, City University of Hong Kong, 83 Tat Chee Avenue, Kowloon, Hong Kong, 999077, China*
[d] *Hong Kong Institute for Clean Energy, City University of Hong Kong, Kowloon 999077, Hong Kong*
[e] *Hong Kong Institute for Advanced Study, City University of Hong Kong, Kowloon, Hong Kong, 999077, China*

† Electronic supplementary information (ESI) available. See DOI: https://doi.org/10.1039/d3ee01362f

Introduction

Charge carriers are fundamental components of batteries that determine battery chemistry and performance.[1] In conventional rechargeable metal anode batteries, the corresponding metal ions serve as the charge carriers and shuttle between the anode and cathode, which requires the cathode materials to allow the reversible intercalation of the metal ions. Thus, the selectivity of cathode materials is severely limited. Recently, hybrid batteries without anode metal ions as the charge carriers have attracted tremendous attention, which has initiated a promising approach for designing batteries with better electrochemical performance and extending the selection of cathode materials. For instance, Na–Li hybrid batteries,[2–4] Mg–Li hybrid batteries,[5–8] Mg–Na hybrid batteries, and calcium-ion-based hybrid batteries exhibited a high operating voltage and stable cycling performance.[9–16]

Aqueous rechargeable zinc-based batteries with the advantages of low-cost, facile manufacturing, and superior safety have been developed *via* employing alkaline, neutral or mild acidic electrolytes, and are the most potential candidates in large-scale and safe energy storage systems. For aqueous zinc batteries with neutral or mild acidic electrolytes, previous reports demonstrate that both H^+ and Zn^{2+} usually act as the charge carriers to intercalate and deintercalate into cathode materials.[17–22] However, due to the high electrode potential of zinc in a neutral or mild acidic electrolyte (−0.76 V *versus* the standard hydrogen electrode (SHE)), the narrow electrochemical stability window (ESW), and the limitation of available cathode materials, zinc batteries usually exhibit a working voltage of below 1.5 V, which vastly limits their applications. Moreover, with Zn^{2+} as the high charge ion, most cathode materials cannot allow its reversible intercalation. Therefore, developing hybrid batteries with non-zinc ions as charge carriers is effective to improve the electrochemical performance of zinc-based batteries. For example, high-voltage materials $LiMn_2O_4$,[23] $LiVPO_4F$,[24] and CuHCF could be used as the cathodes[25] when Li^+ ions or Na^+ ions worked as charge carriers in zinc-based hybrid batteries. Nevertheless, the operating voltages were still below 2 V, which is far lower than that of commercial lithium-ion batteries (LIBs) (>3 V). In alkaline electrolyte, the electrochemical potential of zinc is about −1.21 V *versus* the SHE, which can potentially lead to a higher voltage of zinc-based hybrid batteries. Typically, the traditional commercialized alkaline nickel–zinc battery is a representative Zn^{2+}/H^+ hybrid battery. H^+ serves as the charge carrier and the anodic reaction is the conversion between Zn and ZnO, and moreover, H^+ is reversibly intercalated into the $Ni(OH)_2$ cathode. However, because of the narrow cathodic window and low reduction potential of $Ni(OH)_2$ in alkaline electrolyte, the operating voltage of the battery is also about 1.7 V. In addition, due to the poor compatibility of alkaline electrolyte with most cathode materials, the development of high-voltage zinc-based hybrid batteries based on alkaline electrolytes remains a challenge.

Hence, to take advantage of the low electrochemical potential of zinc in alkaline electrolytes, multi-chamber structured batteries have been developed recently.[26–28] These devices usually consist of alkaline/neutral/acid electrolyte chambers, which could broaden the ESW to be ~3.2 V and achieve working voltages of over 2 V by assembling hybrid batteries. However, the ESWs of multi-chamber alkaline/acid electrolytes are still not sufficiently wide. More importantly, single-phase aqueous electrolytes including alkaline, neutral, and acid electrolytes are inclined to be miscible, leading to a poor stability of the batteries. In addition, the cathodes need to be immersed in the strong acid electrolyte, resulting in their decomposition. Accordingly, many commonly used high voltage materials such as $LiMn_2O_4$, $LiNi_{0.5}Mn_{1.5}O_4$ and $LiCoMnO_4$ cannot work, which limits the further improvement of the operating voltage of zinc batteries.

On the other hand, the growth of zinc dendrites is one of the main failure modes of zinc batteries. In particular, the growth of dendrites in alkaline electrolytes is much more severe than that in acid or neutral electrolytes. Although much effort has been made to constrain the growth of zinc dendrites, they are generally not effective for zinc anodes in alkaline electrolytes.[29–32] An ultimate way to prevent dendrites approaching the cathode is to create an electrolyte structure with no Zn^{2+} ions existing at the cathode side, which has never been demonstrated so far.

Herein, we developed a phase-separation electrolyte (PSE) and for the first time achieved an unprecedented average operating voltage of up to 3.41 V for alkaline aqueous hybrid batteries. The PSE is composed of alkaline aqueous and *N*-methyl-*N*-butylpyrrolidinium bis(trifluoromethylsulfonyl)imide ($Py_{14}TFSI$) electrolytes, which can autonomically form separated aqueous phases and oil phases due to their completely immiscible features. By employing Li^+ as the charge carrier, those cathode materials that do not allow reversible intercalation of Zn^{2+} can be matched with zinc anodes. In addition, experiments, and molecular dynamics (MD) simulations reveal that the PSE has the capability of additionally boosting the working voltage by ~0.35 V *via* interface ion transfer electrochemistry. Moreover, in the PSE, Zn^{2+} ions are completely confined in the aqueous electrolyte, which thoroughly prevents the zinc dendrites from reaching the cathode. As a result, with the $LiNi_{0.5}Mn_{1.5}O_4$ cathode, a record-high average operating voltage of 3.41 V was achieved for zinc/lithium hybrid batteries.

Phase-separation electrolytes

In contrast to the conventional single-phase electrolyte of zinc batteries, the PSE consists of completely immiscible water and oil components for the Zn anode and cathode materials, respectively, as shown in Fig. 1(a) and the ESI,† Fig. S1. The aqueous electrolyte component contains 3 M LiOH, 0.3 M ZnO and 2 M LiTFSI, enabling the reversible plating/stripping of Zn in the alkaline electrolyte. The LiTFSI dissolved in the $Py_{14}TFSI$ as the oil phase component of the PSE, which is totally immiscible with the aqueous phase component. To decrease the viscosity of the $Py_{14}TFSI$, highly fluorinated ether (HFE) of

1,1,2,2-tetrafluoroethyl-2,2,3,3-tetrafluoropropylether that is also immiscible with aqueous electrolytes was employed as the diluent, considering its high stability against alkali compared with the conventional ester solvents (ESI,† Fig. S2). The ionic conductivity was significantly increased from 0.34 ($Py_{14}TFSI$) to 1.23 mS cm^{-1} ($Py_{14}TFSI$-HFE) (ESI,† Fig. S3). The inset in Fig. 1(b) shows the clearly separated two phases autonomically formed in the PSE.

Linear sweep voltammetry (LSV) shows that the pure $Py_{14}TFSI$ decomposes over 2.5 V (*vs.* Ag/AgCl) (ESI,† Fig. S4a), whereas HFE has no obvious decomposition voltage (ESI,† Fig. S4b). After introducing the HFE, the cathodic limitation of the $Py_{14}TFSI$-HFE electrolyte is extended to 2.9 V (*vs.* Ag/AgCl) (Fig. 1(b)). Although the PSE contains an aqueous component, the cathodic window of $Py_{14}TFSI$-HFE in the PSE was unaffected due to the intrinsically immiscible character. The alkaline aqueous electrolyte presents a hydrogen evolution reaction (HER) below −1.6 V (*vs.* SHE). Therefore, the PSE exhibits a remarkable ESW of ~4.6 V (Fig. 1(c)). More importantly, the 2.9 V cathodic window of the PSE enables nearly all current high-potential cathode materials to be usable in zinc batteries (Fig. 1(d)), which forms the foundation of zinc batteries with a super high voltage output.[33–46]

High operating voltage aqueous zinc/lithium hybrid batteries based on PSEs

To investigate the electrochemical behaviors of zinc/lithium hybrid batteries based on the PSE, four high-potential materials

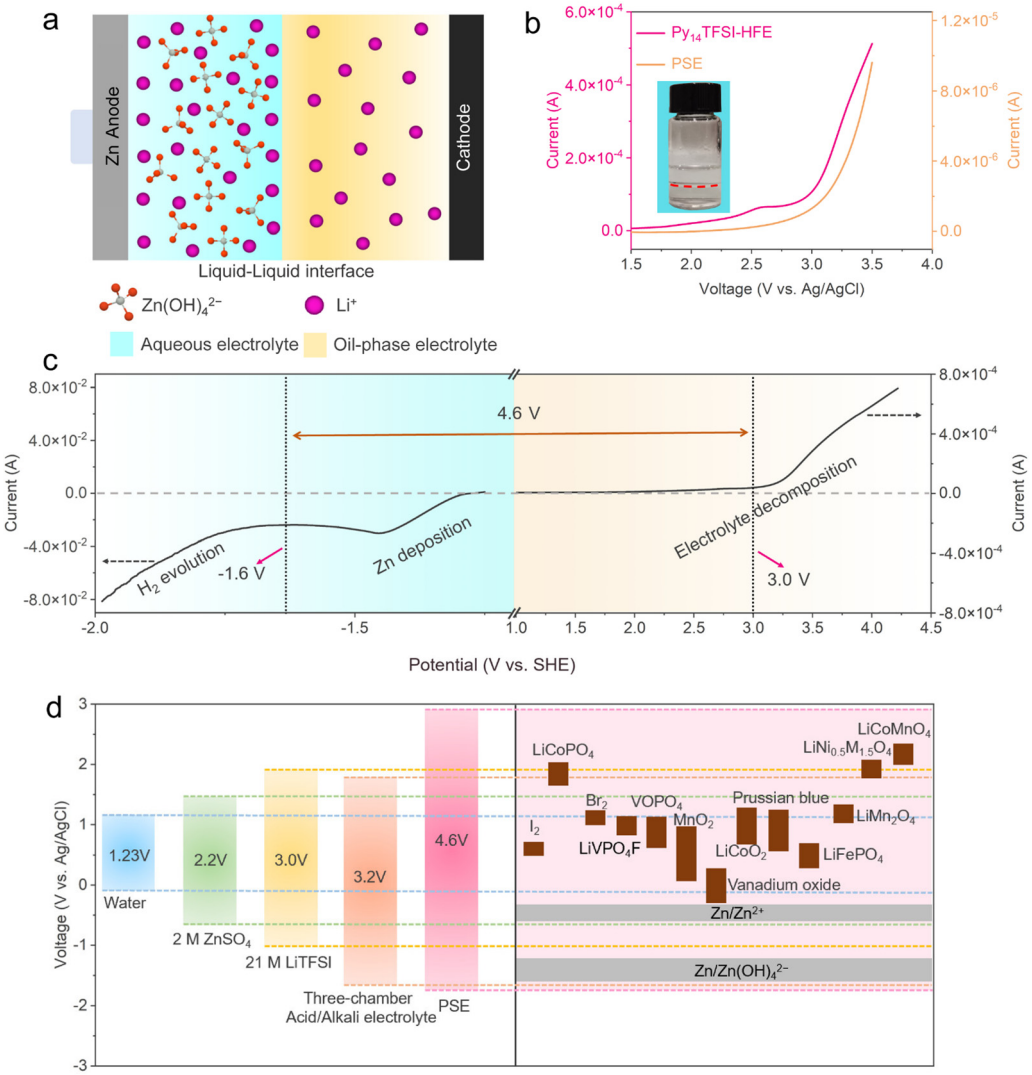

Fig. 1 ESW of the PSE and comparison of cathode materials with different potentials. (a) Schematic illustration of the PSE in zinc batteries. (b) Comparison of the cathodic windows of $Py_{14}TFSI$-HFE and PSE (the inset is the optical image of the PSE, and the dotted red line is the interface of two phases). The LSV was measured at a scanning rate of 5 mV s^{-1}. (c) Verification of the ESW of the PSE. Anodic and cathodic windows were obtained from LSV analysis at a scan rate of 5 mV s^{-1} against a Hg/HgO and Ag/AgCl reference electrode, respectively, wherein the potential has been converted to the SHE references for convenience. (d) Comparison of the ESW of various electrolytes and potentials of materials.

of $LiFePO_4$, $LiMn_2O_4$, $LiNi_{0.5}Mn_{1.5}O_4$ and $LiCoMnO_4$ were employed as cathodes. The reversible electrochemical behavior and galvanostatic voltage profiles of the Zn|PSE|$LiFePO_4$ battery are shown in the ESI,† Fig. S5a and Fig. 2(a), respectively. The well-defined and symmetrical redox peaks of cyclic voltammetry (CV) correspond to the typical ultra-flat discharge and charge plateaus of the $LiFePO_4$. Benefiting from the PSE, even with the $LiFePO_4$ cathode, the Zn|PSE|$LiFePO_4$ can achieve a high open-circuit voltage (OCV) of 2.27 V and average working voltage of 1.85 V at 0.2C, respectively, which exceeds most reported high-voltage zinc batteries. It also delivered a specific capacity of 165.2 mA h g^{-1}, corresponding to a high energy density of 307.3 W h $kg_{cathode}^{-1}$. Fig. 2(b) exhibits the charge–discharge profiles of a Zn|PSE|$LiMn_2O_4$ cell. The cell exhibits a high OCV of up to 2.87 V with two high discharge plateaus at ~2.7 V and ~2.5 V, corresponding to two well-defined anodic peaks of CV curves (ESI,† Fig. S5b). It delivers a high average operating voltage of 2.56 V and a specific capacity of

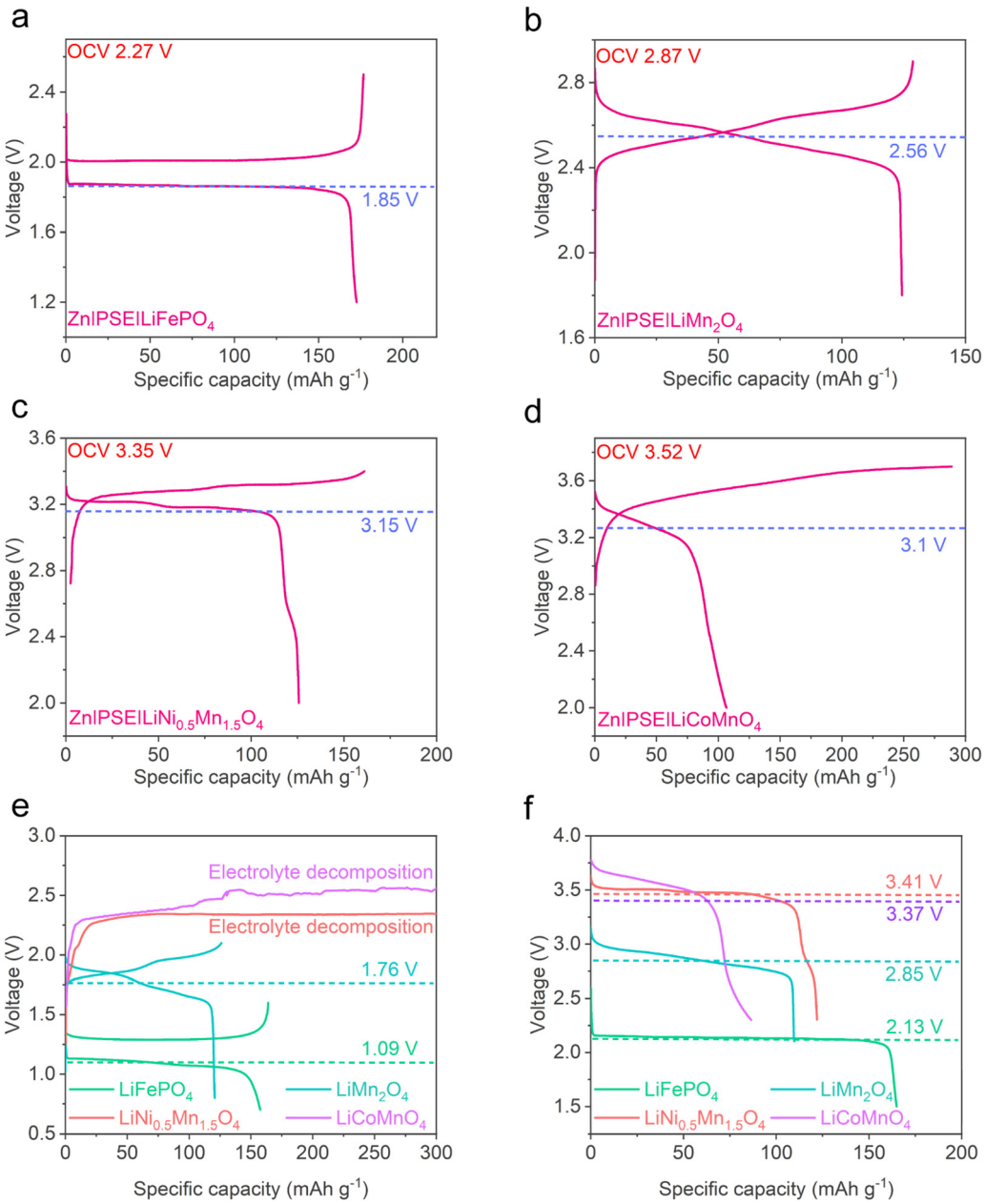

Fig. 2 Electrochemical performances of $LiFePO_4$, $LiMn_2O_4$, $LiNi_{0.5}Mn_{1.5}O_4$ and $LiCoMnO_4$ cathodes in the PSE and the WiS electrolytes. (a)–(d) Typical charge–discharge voltage profiles of Zn|PSE|$LiFePO_4$, Zn|PSE|$LiMn_2O_4$, Zn|PSE|$LiNi_{0.5}Mn_{1.5}O_4$ and Zn|PSE|$LiCoMnO_4$ batteries. The dotted line represents the average operating voltage. (e) The charge–discharge voltage profiles of Zn|WiS|$LiFePO_4$, Zn|WiS|$LiMn_2O_4$, Zn|WiS|$LiNi_{0.5}Mn_{1.5}O_4$ and Zn|WiS|$LiCoMnO_4$ batteries. The dotted line represents the average operating voltage. (f) The discharge profiles of $LiFePO_4$, $LiMn_2O_4$, $LiNi_{0.5}Mn_{1.5}O_4$ and $LiCoMnO_4$ cathodes with the PSE consisting of the concentrated alkaline aqueous component. The dotted lines represent the average operating voltages.

122 mA h g^{-1}. Furthermore, the Zn|PSE|$LiNi_{0.5}Mn_{1.5}O_4$ cell exhibits an OCV up to 3.35 V and discharge plateaus at about 3.2 V (Fig. 2(c), corresponding to the CV shown in the ESI,† Fig. S5c), consistent with the typical discharge behavior of $LiNi_{0.5}Mn_{1.5}O_4$. Benefiting from the high discharge plateaus, the average operating voltage could reach an unprecedented 3.15 V at 0.2C and a high energy density of 396 W h $kg_{cathode}^{-1}$ is obtained. Fig. 2(d) shows the charge–discharge profiles of a Zn|PSE|$LiCoMnO_4$ cell. The Zn|PSE|$LiCoMnO_4$ battery discharges from 3.52 V and delivers a high plateau at 3.3 V, corresponding well to the reduction peak of CV (ESI,† Fig. S5d). The average discharge voltage is up to 3.10 V, which is slightly lower than that of the Zn|PSE|$LiNi_{0.5}Mn_{1.5}O_4$ battery due to more capacity being discharged at 2.0–3.2 V. Apparently, benefiting from the immiscible design of the PSE, the aqueous zinc/lithium hybrid batteries exhibited excellent compatibility for a variety of cathode materials and for the first time achieved a landmark average operating voltage of over 3 V.

Water-in-salt (WiS) electrolytes with extended ESWs were widely used to achieve high voltages for zinc-based hybrid batteries.[23,24] For comparison, we tested the electrochemical performance of zinc batteries with the same cathode materials in the WiS electrolyte. As shown in Fig. 2(e), the Zn|WiS|Li-$FePO_4$ battery exhibited flat discharge/charge plateaus corresponding well to the CV profile (ESI,† Fig. S6a). Nevertheless, it only demonstrated a 1.09 V working voltage in the 1 M zinc trifluoromethylsulfonate ($Zn(OTF)_2$) in 21 M LiTFSI electrolyte at 0.2C, which is far below the achieved 1.85 V in the PSE. Similarly, the CV result (ESI,† Fig. S6b) and galvanostatic discharge profile (Fig. 2(e)) demonstrate that the Zn|WiS|$LiMn_2O_4$ battery with the WiS electrolyte exhibited two discharge plateaus at 1.9 and 1.7 V, respectively, and the average discharge voltage is only 1.76 V. As for the $LiNi_{0.5}Mn_{1.5}O_4$, although the WiS electrolyte possesses an extended electrochemical window of $\sim$3.1 V (ESI,† Fig. S7), obvious decomposition of electrolyte could be observed after charging to 2.3 V (Fig. 2(e)). This is due to the strong catalytic effect of Ni^{4+}, leading to the oxygen evolution. The Zn|WiS|$LiCoMnO_4$ battery also shows inevitable decomposition of water due to the catalytic effects of Co^{4+}(Fig. 2(e)). Accordingly, the sharp contrast indicates the PSE can make the best advantage of the electrode potential of Zn in an alkaline environment and avoid the negative effects of alkaline electrolyte on cathode materials, rendering the alkaline zinc/lithium hybrid batteries with remarkable voltage outputs. In addition, the unconventional PSE with the 4.6 V electrochemical window provides excellent flexibility in selecting high potential cathode materials.

Since the concentration of alkali will affect the electrode potential of zinc due to the Nernst shift, the working voltage of the zinc/lithium hybrid batteries with PSEs can be regulated *via* adjusting the aqueous phase components of the PSE. As shown in Fig. 2(f), after improving the concentration of alkali, even the Zn‖$LiFePO_4$ cell can achieve an average discharge voltage of 2.13 V at 0.2C. For the Zn‖$LiMn_2O_4$ battery in the concentrated alkaline PSE, the two discharge plateaus were further boosted to 2.95 V and 2.75 V, respectively, and it delivered a 3.12 V OCV and a high operating voltage of 2.85 V. The discharge plateau of Zn‖$LiNi_{0.5}Mn_{1.5}O_4$ in the concentrated alkaline PSE reaches an unprecedented 3.5 V, and the average operating voltage is enhanced to 3.41 V, which is almost twice that of most high-voltage zinc batteries and comparable with rechargeable LIBs. Similarly, the discharge plateau and average operating voltage of the Zn‖$LiCoMnO_4$ battery were improved to 3.6 V and 3.37 V, respectively (Fig. 2(f)).

Energy storage mechanism of cathode materials in the PSE

It should be noted that our investigation and previous reports demonstrated that the Zn‖$LiFePO_4$ and the Zn‖$LiNi_xMn_{2-x}O_4$ can cycle in the Li^+/Zn^{2+} hybrid aqueous electrolytes. In this case, Li^+ instead of Zn^{2+} intercalates to cathodes.[23,47,48] However, in an organic electrolyte, we found the Zn‖$LiFePO_4$ and Zn‖$LiNi_xMn_{2-x}O_4$ are not reversible anymore. As shown in Fig. 3(a), in a 0.4 M LiTFSI/0.2 M $Zn(TFSI)_2$ based Py_{14}TFSI-HFE electrolyte, only 15% of the theoretical capacity was delivered and the battery failed after 5 cycles, demonstrating the irreversible intercalation of Zn^{2+}. A similar phenomenon was observed for the Zn‖$LiMn_2O_4$ battery with the same electrolyte (Fig. 3(b)).

To explain this phenomenon, radial distribution functions (RDFs) were employed to analyze the priority of Li^+ and Zn^{2+} ions into cathode materials in aqueous and organic electrolytes. As shown in Fig. 3(c), H_2O molecules mainly occupy the first coordination shell of both Li^+ and Zn^{2+} in a 0.2 M $Zn(OTF)_2$/0.4 M LiTFSI aqueous electrolyte. The coordination numbers of Zn^{2+} are higher than those of Li^+ and the interaction of H_2O molecules with Zn^{2+} is stronger than that of Li^+, revealed by the larger $g(r)$. This result suggests that Li^+ will preferentially intercalate the cathode materials. Even in the 1 M $Zn(OTF)_2$/21 M Zn TFSI based WiS electrolyte (Fig. 3(d)), due to the high molar ratio of salt, H_2O molecules and $TFSI^-$ occupy the first coordination shell of both Li^+ and Zn^{2+}. However, compared to Zn^{2+}, the larger $g(r)$ indicates that Li^+ ions will still preferentially intercalate to the cathode materials. The same results can be obtained even by substituting the $Zn(OTF)_2$ with $Zn(TFSI)_2$ (ESI,† Fig. S8). In sharp contrast, for the organic Py_{14}TFSI-HFE electrolyte (Fig. 3(e)), the first coordination shell was enriched with $TFSI^-$ and HFE molecules for both Li^+ and Zn^{2+}. The larger $g(r)$ of Li^+ indicates the interaction between Li^+ and electrolyte is stronger, demonstrating that Zn^{2+} instead of Li^+ will preferentially intercalate the cathode materials. Therefore, both the experimental and simulation results reveal that the irreversible intercalation of Zn^{2+} is the reason leading to the failure of $LiFePO_4$ and $LiNi_xMn_{2-x}O_4$ cathodes in organic electrolytes. The hybrid batteries that lithium ions serve as the charge carriers is the only approach to use these kinds of materials.

In our PSE, due to the strong coordination between Zn^{2+} and OH^- (the stability constant of $Zn(OH)_4^{2-}$ is about 10^{-14}),[49] Zn^{2+} ions are completely confined in the aqueous electrolyte. The

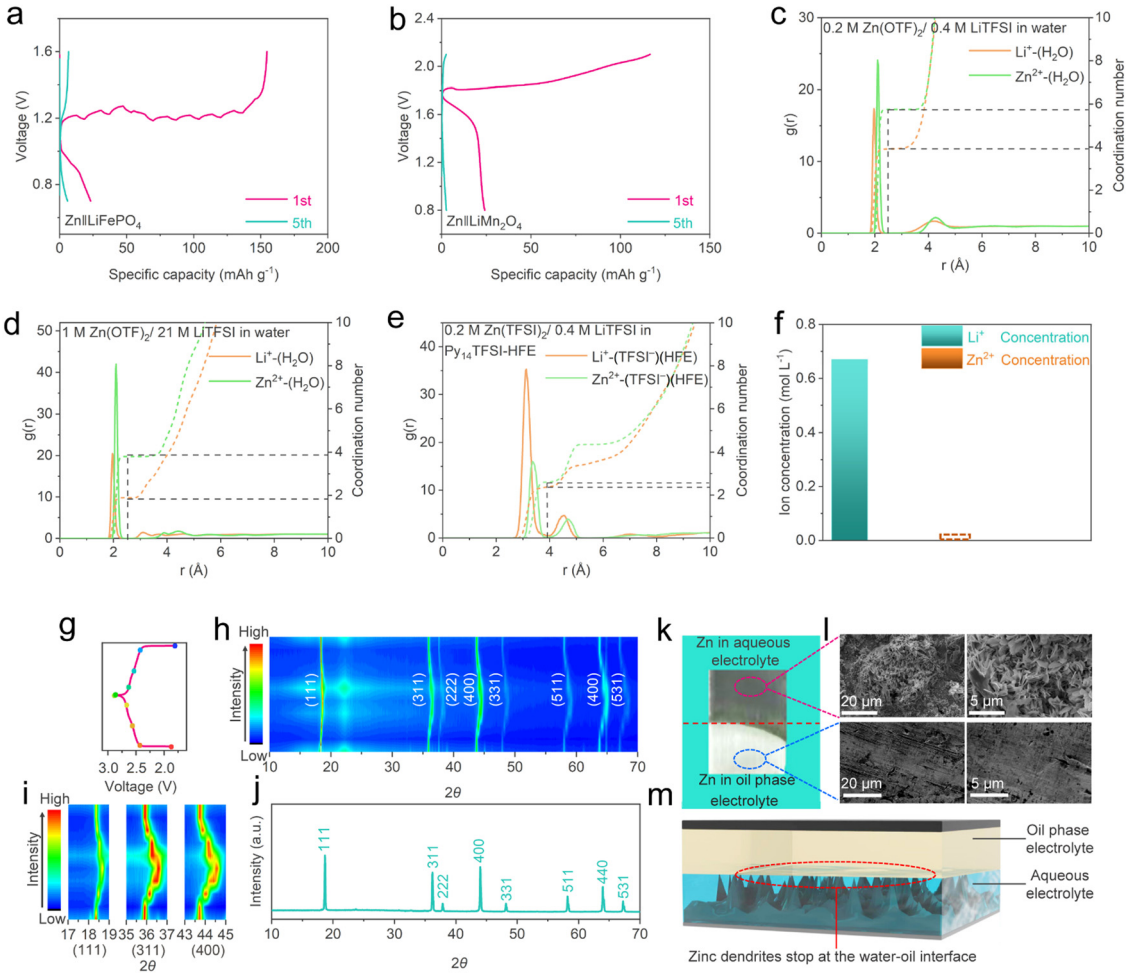

Fig. 3 The mechanisms of energy storage and interfacial inhibition of Zn dendrites in the PSE. (a) and (b) The charge–discharge voltage profiles of Zn‖$LiFePO_4$ and Zn‖$LiMn_2O_4$ batteries with the Py_{14}TFSI-HFE electrolyte at the 1st and 5th cycles. (c) Radial distribution functions of Li^+–(H_2O) and Zn^{2+}–(H_2O) pairs in 0.2 M $Zn(OTF)_2$/0.4 M LiTFSI dissolved aqueous electrolyte. (d) Radial distribution functions of Li–(H_2O) and Zn–(H_2O) pairs in 1 M $Zn(OTF)_2$/21 M LiTFSI dissolved aqueous electrolyte. (e) Radial distribution functions of Li–($TFSI^-$)(HFE) and Zn–($TFSI^-$)(HFE) pairs in 0.2 M $Zn(TFSI)_2$/0.4 M LiTFSI dissolved Py_{14}TFSI-HFE electrolyte. (f) ICP result of the oil phase component of the PSE. (g) The cathode electrodes at various charge and discharge states for *ex situ* XRD tests. (h) The contour plot of the corresponding XRD patterns. (i) The contour plots of selected typical peaks of (111), (311) and (400). (j) The XRD pattern of the initial $LiMn_2O_4$ power. (k) Optical image of the Zn anode after cycling. The dark grey part was immersed in the aqueous phase component of the PSE, and the silvery part was immersed in the oil phase part of the PSE. (l) SEM images of Zn anode surfaces in the aqueous phase and oil phase components of the PSE, respectively. (m) Schematic illustration of Zn dendrite growth stopping at the interface.

entering of Zn^{2+} ions to Py_{14}TFSI-HFE is effectively blocked at the interface. As shown in Fig. 3(f), the inductively coupled plasma (ICP) results show that Zn^{2+} ions hardly exist in the oil-phase electrolyte, which enables the selected four cathode materials be cycled with the PSE electrolyte since only Li^+ ions serve as the charge carriers in the Py_{14}TFSI-HFE components of the PSE. The Li^+ ions deintercalation and intercalation reactions in the cathode materials in the PSE during the charge–discharge process were also verified by X-ray diffraction (XRD) measurement. As shown in Fig. 3(g) and (h), the *ex situ* XRD patterns of $LiMn_2O_4$ were collected between 1.8 and 2.9 V during the charge–discharge process. The Bragg peaks ranging from 10 and 70° exhibit a continuous shift during the entire charge–discharge process, which is consistent with contraction and expansion of the unit cells of $LiMn_2O_4$ during Li extraction and insertion,[50–52] indicating no Zn^{2+} inserted (Fig. 3(h)). The typical (111), (311) and (400) peaks gradually broaden during charge and recover to the standard $LiMn_2O_4$ structure with the intercalation of Li^+, indicating a reversible ion intercalation/deintercalation with the PSE (Fig. 3(i) and (j)). Similarly, the *ex situ* XRD results of $LiFePO_4$, $LiNi_{0.5}Mn_{1.5}O_4$ and $LiCoMnO_4$ also exhibited the same reversible phase transformation in the PSE as in the conventional organic electrolytes (ESI,† Note S1 and Fig. S9–S11).

Another merit of our PSE is its ability to completely avoid Zn dendrites approaching the cathode side of the battery. The growth of zinc dendrites is a great challenge for zinc batteries because it will lead to the short circuit and battery failure. In particular, the growth of zinc dendrites in alkaline solution is much more severe than that in neutral or acid electrolyte. While

many strategies have been proposed to suppress dendrites growth in mild electrolytes, they are generally not effective at all when the electrolytes are switched to alkaline ones. In our PSE, since Zn^{2+} ions hardly exist in the organic Py_{14}TFSI-HFE component, the plating of zinc can only be processed in the aqueous phase component during charge, suggesting that the zinc dendrites cannot grow across the water–oil interface. To verify our inference, the zinc anode was put across the water–oil interface and carried out the electrochemical measurements. As shown in Fig. 3(k), after 10 cycles, the plating of zinc only occurred in the aqueous phase component of the PSE, and the zinc metal in the oil-phase electrolyte maintains a smooth surface. Scanning electron microscopy (SEM) images reveal the surface morphologies of the zinc anode. As shown in Fig. 3(l), obvious zinc dendrites and nanosheets can be observed for the zinc anode immersed in the aqueous phase component of the PSE. In sharp contrast, the images of the zinc anode in the organic Py_{14}TFSI-HFE component of the PSE demonstrate a pristine surface with no zinc plated, which confirms our inference that the zinc dendrites cannot grow across the water–oil interface (Fig. 3(m)), completely avoiding the dendrite induced short circuit.

Interface induced voltage enhancement by the PSE

The developed PSE electrolyte endows alkaline zinc/lithium batteries with unprecedent voltage outputs. However, detailed calculations reveal a deviation of theoretical voltages from the obtained voltages, that is, the obtained voltages are even higher than the theoretical voltages if only the potential difference of the cathode and anode is considered. As shown in the ESI,† Fig. S12a and b, the symmetric redox peak of $LiFePO_4$ is located at 3.33 V (*vs.* Li^+/Li) in the Py_{14}TFSI-HFE electrolyte, and the average discharge voltage of the $LiFePO_4$ cathode is ~0.3 V (*vs.* SHE) at 0.2C. Considering the oxidation potential of the zinc anode in 3 M LiOH electrolyte is −1.23 V (*vs.* SHE) (ESI,† Fig. S13), accordingly, the theoretical average operating voltage of the Zn‖$LiFePO_4$ should be ~1.53 V, which is far below the experimental result of 1.85 V. Similarly, for the $LiMn_2O_4$ cathode, two redox peaks located at 4.1 and 3.9 V (*vs.* Li^+/Li), correspond to the two well-defined discharge plateaus (ESI,† Fig. S12c and d). The average discharge voltage is ~0.98 V (*vs.* SHE) for $LiMn_2O_4$ in the Py_{14}TFSI-HFE electrolyte. This indicates that the two discharge plateaus of the Zn‖$LiMn_2O_4$ cell should be at 2.3 and 2.1 V, and the average operating voltage is ~2.21 V, while it achieves 2.56 V in the PSE. Similarly, based on the CV measurements and galvanostatic discharge test results (ESI,† Fig. S12e–h), the high-potential $LiNi_{0.5}Mn_{1.5}O_4$ and $LiCoMnO_4$ material-based zinc/lithium hybrid batteries should have 2.8 and 2.75 V average working voltages, respectively, much less than the >3 V achieved.

We note that all average operating voltages of the zinc/lithium hybrid batteries in the PSE are generally 0.35 V higher than the theoretical values. To clarify the mechanism of the voltage enhancement, MD studies were performed. Fig. 4(a) and (b) exhibit the distribution of Li^+ and $TFSI^-$ ions near the liquid–liquid interface in the PSE in the static and discharge states, and the corresponding snapshots of the cross section of the liquid–liquid interface are shown in the ESI,† Fig. S14 and S15. In the static state, the density of Li^+ ions reaches 3 nm^{-3} within 1 nm from the interface in the aqueous component of the PSE (Fig. 4(c)). During discharge, $TFSI^-$ and Li^+ ions move towards the anode and cathode, respectively. Apparently, Li^+ ions accumulate at the aqueous electrolyte side, while $TFSI^-$ ions also diffuse across the liquid–liquid interface and accumulate at the aqueous side of the PSE, which can be attributed to the different transport velocities of ions in the aqueous phase and oil phase components of the PSE. Accordingly, the number density of Li^+ ions increases significantly within 1 nm from the interface and dramatically decreases within 2–4 nm from the interface during discharge (Fig. 4(c)). $TFSI^-$ ions also increase at the aqueous side compared to that in the static state (ESI,† Fig. S16). Therefore, the equilibrium state of the LiTFSI in the aqueous phase and oil phase components of the PSE is broken at the interface, leading to a remarkable concentration increase of LiTFSI in the aqueous phase component of PSE close to the interface. The concentration gradient will drive LiTFSI to spontaneously diffuse into the oil phase component of the PSE to maintain the balance.

Experimentally, a four electrode cell is a powerful tool to investigate ion transfer electrochemistry across the liquid–liquid interface. The CV result demonstrated that the ion transfer potential of Li^+ from the aqueous component to the oil phase component of the PSE is about 0.38 V (Fig. 4(d)). In our PSE, since the Zn^{2+} ions are confined in the aqueous component, Li^+ ions serve as the charge carriers during the charge–discharge process. The results indicate the solvation energy of Li^+ in the oil phase component is higher than that in the aqueous component. Density functional theory (DFT) calculation also demonstrated that Li^+ ions are in a high energy state in the oil phase component (ESI,† Fig. S17). Four H_2O molecules interact with a Li^+ ion in the first solvation sheath in the aqueous components, and $TFSI^-$ and two HFE molecules interact with a Li^+ ion in the first solvation sheath in the oil phase component ($Li^+(TFSI^-HFE_2)$). Since the cathode materials are placed in the oil phase component, the Li^+ can directly desolvate from the high energy state and intercalate into the cathode materials (Fig. 4(e)), which contributes to the additional enhancement of the operating voltage. Meanwhile, according to the above MD results, the concentration gradient at the interface during discharge can drive the Li^+ ions to diffuse into the oil phase electrolyte, leading to a stable voltage increase without breaking the ionic equilibrium in the PSE.

As shown in Fig. 4(f), with the addition of 0.35 V boosted by the interface in PSE, the average operating voltages of Zn‖$LiFePO_4$, Zn‖$LiMn_2O_4$, Zn‖$LiNi_{0.5}Mn_{1.5}O_4$ and Zn‖$LiCoMnO_4$ with the concentrated alkaline PSE were significantly enhanced by 41.1%, 30.0%, 21.3% and 20.7%, respectively, compared with the corresponding theoretical values by only considering the potential difference of the anode and cathode. In addition,

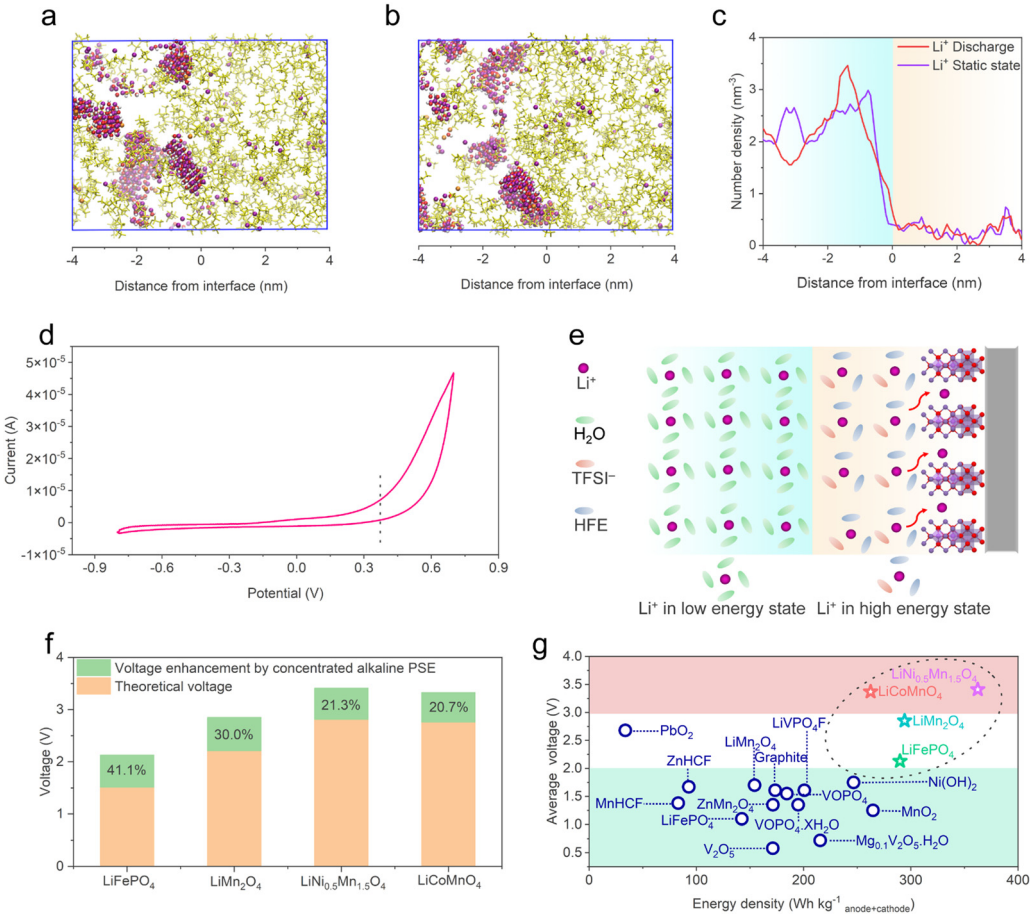

Fig. 4 Additional voltage enhancement in the PSE by interface ion transfer electrochemistry and comparison of various zinc batteries. (a) Snapshot of the liquid–liquid interface at the static states. Purple ball: Li^+, orange ball: Zn^{2+}, red and white ball: OH^-, yellow: $TFSI^-$. (b) Snapshot of the liquid–liquid interface during discharge. (c) Comparison of the number density of Li^+ ions at the liquid–liquid interface. (d) CV of Li^+ ion transfer across the liquid–liquid interface at a scan rate of 20 mV s^{-1}. Measurement was carried out with a four-electrode system. (e) The scheme of the desolvation of Li^+ ions in the oil phase and into the cathode material. (f) The percentage of voltage increase of Zn‖$LiFePO_4$, Zn‖$LiMn_2O_4$, Zn‖$LiNi_{0.5}Mn_{1.5}O_4$ and Zn‖$LiCoMnO_4$ batteries in the concentrated alkali PSE, respectively, in comparison to the theoretical operating voltages when only the potential differences of the electrodes are considered. (g) The average operating voltages and energy densities of Zn‖$LiFePO_4$, Zn‖$LiMn_2O_4$, Zn‖$LiNi_{0.5}Mn_{1.5}O_4$ and Zn‖$LiCoMnO_4$ batteries based on the PSE, compared with the reported cathode materials of zinc batteries. All energy densities were calculated using the total mass of the anode and cathode electrodes at N/P = 1. The red region and green region represent the operating voltages of LIBs and aqueous batteries, respectively.

benefiting from the high operating voltages, the energy densities of four zinc/lithium hybrid batteries in our work were all over 300 W h $kg_{cathode}^{-1}$, and the Zn‖$LiNi_{0.5}Mn_{1.5}O_4$ cell with PSE delivered a high energy density of up to 416 W h $kg_{cathode}^{-1}$.

It should be noted that, for a battery, although the energy density can be improved by increasing either the discharge capacity or operating voltage, the voltage enhancement has distinct advantages on improving the energy density of a battery compared with discharge capacity enhancement when the anode is considered. For example, a cathode material with 410 mA h g^{-1} capacity and 0.8 V voltage output needs at least 0.5 g Zn to match, while a cathode material with 205 mA h g^{-1} capacity and 1.6 V voltage output only needs 0.25 g Zn to couple. Fig. 4(g) exhibits the energy densities of the reported main cathode materials in zinc batteries (based on the mass of both zinc anode and cathode materials, and N/P is assumed to be 1).[24,37,38,53–62] The operating voltages of most of the zinc batteries are located in the green zone (below 2 V). The red zone represents the region that can only be achieved by the organic LIBs previously. Benefiting from the PSE, the zinc/lithium hybrid batteries exhibited high operating voltages comparable to that of LIBs, and the high operating voltages enable the energy density based on the mass of both the anode and cathode to be maximally utilized. As a result, all batteries with the PSE could deliver high energy densities over 250 W h $kg_{anode+cathode}^{-1}$ and an energy density of 362.4 W h $kg_{anode+cathode}^{-1}$ was achieved by the Zn‖$LiNi_{0.5}Mn_{1.5}O_4$ cell.

Rate and cycling performance

To evaluate the electrochemical stability of zinc/lithium hybrid batteries with the PSE, the developed batteries were tested at 1C for over 50 cycles (ESI,† Fig. S18). Compared with the

$LiNi_{0.5}Mn_{1.5}O_4$ and the $LiCoMnO_4$, the commercialized $LiFePO_4$ and $LiMn_2O_4$ exhibit better cycling stability. This is because the $LiNi_{0.5}Mn_{1.5}O_4$ and $LiCoMnO_4$ materials usually need coating or additives in the electrolyte to form a stable cathode electrolyte interface (CEI).[63–67] The Zn|PSE|$LiFePO_4$ and Zn|PSE|$LiMn_2O_4$ batteries delivered high discharge capacities of 151.4 and 100.1 mA h g^{-1} in over 50 cycles, respectively. SEM images of the $LiMn_2O_4$ and $LiFePO_4$ before and after cycling are shown in the ESI,† Fig. S19 and S20. Although $LiNi_{0.5}Mn_{1.5}O_4$ and $LiCoMnO_4$ cathodes did not exhibit a remarkable cycling stability, the morphologies of $LiNi_{0.5}Mn_{1.5}O_4$ and $LiCoMnO_4$ still remained unchanged before and after cycling (ESI,† Fig. S21 and S22). Accordingly, the high voltage $LiMn_2O_4$ as a representative cathode was used to further investigate the electrochemical stability of the zinc/lithium hybrid batteries with the PSE. As shown in Fig. 5(a), the rate performance of the Zn|PSE|$LiMn_2O_4$ battery was evaluated from 0.2 to 3C. The battery delivered a specific capacity of 124.3, 115, 114.4, 107.4, 102.7, 92.1, 74.5 and 52.1 mA g^{-1} at 0.2, 0.5, 0.75, 1, 1.5, 2, 2.5 and 3C, respectively. Fig. 5(b) shows the corresponding charge–discharge profiles of the Zn|PSE|-$LiMn_2O_4$ at different rates. Even at a high rate of 3C, the Zn|PSE|$LiMn_2O_4$ battery still exhibits a high working voltage of 2.2 V. In addition, the rate performance of the $LiMn_2O_4$ cathode in the single-phase Py_{14}TFSI-HFE electrolyte was also evaluated with the lithium anode at the same rates (ESI,† Fig. S23a and b). The Li|Py_{14}TFSI-HFE|$LiMn_2O_4$ battery indicates that the rate performance of cathode materials in the PSE mainly depends on the oil phase component. However, the high discharge capacity of the cell at a high rate can be obtained by constant voltage charging (ESI,† Fig. S24). Fig. 5(c) exhibits the long-term cycling performance of the Zn|PSE|-$LiMn_2O_4$ battery at 3C. The battery delivered an initial discharge capacity of 55 mA g^{-1} and maintained about 60 mA g^{-1} capacity after over 600 cycles, indicating the excellent cycling performance of the Zn|PSE|$LiMn_2O_4$ battery. The average coulombic efficiency is over 99.6%, which is even higher than most of the zinc batteries with single-phase electrolytes, and the average operating voltage remained unchanged over 600 cycles (ESI,† Fig. S25). The cycling performance of the Zn‖$LiMn_2O_4$ with concentrated alkaline PSE was also evaluated and the results are shown in the ESI,† Fig. S26. For the zinc/lithium hybrid battery with the zinc anode in PSE, the capacity is determined by the solubilities of the ZnO in the aqueous electrolyte solutions, which limits its further practical application. For commercial zinc–nickel batteries, due to H^+ as the charge carrier, ZnO is employed as the anode to meet the requirements of high areal capacity and practical application.

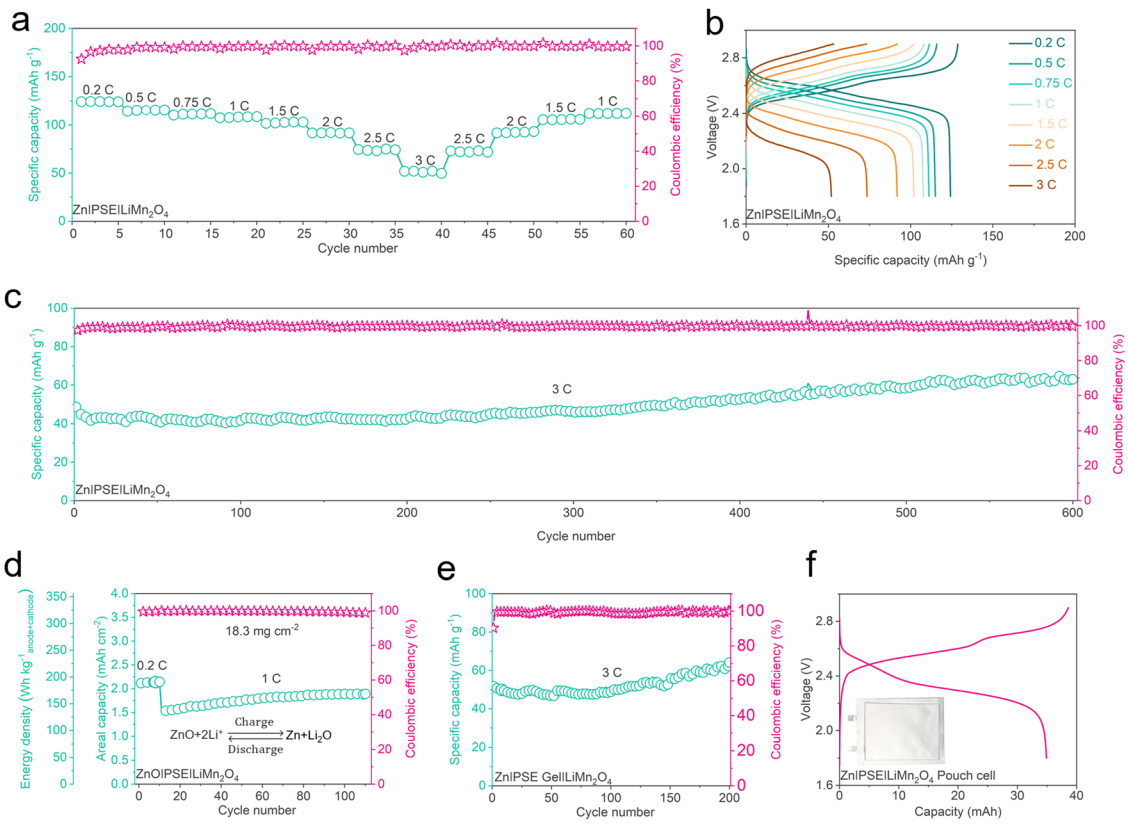

Fig. 5 Electrochemical performance of the Zn‖$LiMn_2O_4$ with PSE. (a) Rate performance of the Zn|PSE|$LiMn_2O_4$ cell. (b) Corresponding charge–discharge profiles at different rates. (c) The cycling stability and coulombic efficiency of the Zn|PSE|$LiMn_2O_4$ cell at 3C. (d) The cycling performance of the cell using the ZnO anode and a high cathode loading mass of 18.3 mg cm^{-2} and the energy densities based on the total weight of the anode and cathode. (e) The cycling performance of the Zn‖$LiMn_2O_4$ cell with gel electrolyte at 3C. (f) The charge–discharge profile of a Zn|PSE|$LiMn_2O_4$ pouch cell.

Accordingly, to evaluate the practical potential of the PSE, a ZnO anode and a $LiMn_2O_4$ cathode with a high cathode loading mass of 18.3 mg cm^{-2} were assembled. As shown in Fig. 5(d), the high capacity ZnO|PSE|$LiMn_2O_4$ cell was first cycled at 0.2C, and it delivered a high areal capacity of 2.14 mA h cm^{-2}. The electrochemical reaction process is similar to the zinc–nickel batteries. Li^+ replaces H^+ as charge carriers, and ZnO is reduced to Zn and Li_2O during charging, so the discharge capacity of the cell is determined by the mass of the electrode materials. The corresponding charge–discharge profiles at 0.2C is shown in the ESI,† Fig. S27. After 10 cycles, the discharge rate was changed into 1C, and the battery could still deliver a high specific capacity of 84 mA h g^{-1} and maintained an areal capacity of $\sim$1.88 mA h cm^{-2} after over 110 cycles with an average coulombic efficiency over 99.6%. Benefiting from the high operating voltage of the PSE based batteries, the energy density of the full cell could reach a high level of 191.3 W h $kg_{anode+cathode}^{-1}$ (the N/P ratio is 1.52). In addition, we also fabricated a cell with gel electrolyte, as illustrated in the ESI,† Fig. S28. It delivered a specific capacity of 61.6 mA h g^{-1} after 200 cycles (Fig. 5(e)), and the pouch cell with gel electrolyte delivers a 35 mA h discharge capacity (Fig. 5(f)).

Conclusion

In summary, we developed a novel and unique phase-separation electrolyte consisting of completely immiscible aqueous phase and oil-phase components. The alkaline aqueous electrolyte takes advantage of the lower electrode potential of the Zn anode and the oil phase Py_{14}TFSI-HFE electrolyte remarkably extends the selection of cathode materials. In addition, the interface ion transfer electrochemistry further boosts the operating voltage by $\sim$0.35 V. Zn^{2+} ions were confined in the aqueous electrolyte *via* the strong coordination effect between Zn^{2+} and OH^-, ultimately eliminating the Zn dendrites approaching the cathode and meanwhile avoiding the irreversible Zn^{2+} intercalation to the cathode. The oil phase electrolyte has excellent compatibility with various cathode materials compared to single phase aqueous electrolytes and the cathodic limitation is extended to 2.9 V. As a result, the zinc/lithium hybrid batteries achieved a record-high average operating voltage comparable to those of LIBs, up to 3.41V, and it delivers a high energy density of 362.4 W h $kg_{anode+cathode}^{-1}$ (N/P is assumed to be 1). The Zn|PSE|$LiMn_2O_4$ delivers an excellent cycle performance over 600 cycles with a 99.6% coulombic efficiency. In addition, the full cell with a commercial level cathode loading of 18.3 mg cm^{-2} delivered a high areal capacity of 2.14 mA h cm^{-2}. The unconventional electrolyte system provides a new approach to fabricate high performance zinc-based batteries and may be used for other battery systems to achieve extraordinary voltage output.

Author contributions

Conceptualization: A. C.; methodology: A. C., Y. Q. Z., Q. L., G. J. L., and S. Y.; investigation: A. C., Y. Q. Z., Z. D. H., Q. Y., X. L. L., H. H., Z. C., J. F., and C. Y. Z.; computation: Y. Q. C.; writing – original draft: A. C. and C. Y. Z.; writing review and editing: A. C., Y. Q. Z., Q. L., G. J. J., S. Y., Z. D. H., Q. Y., H. H., X. L. L, Z. C., J. F., and C. Y. Z.; J. F., and C. Y. Z. jointly supervised this work.

Conflicts of interest

The authors declare no competing interests.

Acknowledgements

This research was supported by the National Key R&D Program of China under Project 2019YFA0705104 and CRF under Project C1002-21G funded by RGC.

References

1 G. Liang, F. Mo, X. Ji and C. Zhi, *Nat. Rev. Mater.*, 2021, **6**, 109–123.
2 J. Z. Guo, Y. Yang, D. S. Liu, X. L. Wu, B. H. Hou, W. L. Pang, K. C. Huang, J. P. Zhang and Z. M. Su, *Adv. Energy Mater.*, 2018, **8**, 1702504.
3 L. Liang, X. Li, F. Zhao, J. Zhang, Y. Liu, L. Hou and C. Yuan, *Adv. Energy Mater.*, 2021, **11**, 2100287.
4 Q. Zhang, Y. Lu, L. Miao, Q. Zhao, K. Xia, J. Liang, S. L. Chou and J. Chen, *Angew. Chem., Int. Ed.*, 2018, **57**, 14796–14800.
5 Q. D. Truong, M. Kempaiah Devaraju, Y. Nakayasu, N. Tamura, Y. Sasaki, T. Tomai and I. Honma, *ACS Omega*, 2017, **2**, 2360–2367.
6 T. Gao, F. Han, Y. Zhu, L. Suo, C. Luo, K. Xu and C. Wang, *Adv. Energy Mater.*, 2015, **5**, 1401507.
7 X. Sun, V. Duffort and L. F. Nazar, *Adv. Sci.*, 2016, **3**, 1600044.
8 Y. Wang, C. Wang, X. Yi, Y. Hu, L. Wang, L. Ma, G. Zhu, T. Chen and Z. Jin, *Energy Storage Mater.*, 2019, **23**, 741–748.
9 J. Lang, C. Jiang, Y. Fang, L. Shi, S. Miao and Y. Tang, *Adv. Energy Mater.*, 2019, **9**, 1901099.
10 N. Wu, W. Yao, X. Song, G. Zhang, B. Chen, J. Yang and Y. Tang, *Adv. Energy Mater.*, 2019, **9**, 1803865.
11 Y. Tang, X. Li, H. Lv, W. Wang, Q. Yang, C. Zhi and H. Li, *Angew. Chem., Int. Ed.*, 2021, **133**, 5503–5512.
12 M. Rashad, M. Asif, Y. Wang, Z. He and I. Ahmed, *Energy Storage Mater.*, 2020, **25**, 342–375.
13 P. Wang and X. Yan, *Energy Storage Mater.*, 2022, **45**, 142–181.
14 Y. Li, Q. An, Y. Cheng, Y. Liang, Y. Ren, C.-J. Sun, H. Dong, Z. Tang, G. Li and Y. Yao, *Nano Energy*, 2017, **34**, 188–194.
15 Y. Xu, W. Cao, Y. Yin, J. Sheng, Q. An, Q. Wei, W. Yang and L. Mai, *Nano Energy*, 2019, **55**, 526–533.
16 Y. Yang, S. Guo, Y. Pan, B. Lu, S. Liang and J. Zhou, *Energy Environ. Sci.*, 2023, **16**, 2358–2367.
17 J. Zhang, W. Li, J. Wang, X. Pu, G. Zhang, S. Wang, N. Wang and X. Li, *Angew. Chem., Int. Ed.*, 2023, **62**, e202215654.

18 Y. Yuan, R. Sharpe, K. He, C. Li, M. T. Saray, T. Liu, W. Yao, M. Cheng, H. Jin and S. Wang, *Nat. Sustain.*, 2022, **5**, 890–898.
19 X. Xie, J. Li, Z. Xing, B. Lu, S. Liang and J. Zhou, *Natl. Sci. Rev.*, 2023, **10**, nwac281.
20 V. Mathew, B. Sambandam, S. Kim, S. Kim, S. Park, S. Lee, M. H. Alfaruqi, V. Soundharrajan, S. Islam and D. Y. Putro, *ACS Energy Lett.*, 2020, **5**, 2376–2400.
21 T. Lv, G. Zhu, S. Dong, Q. Kong, Y. Peng, S. Jiang, G. Zhang, Z. Yang, S. Yang and X. Dong, *Angew. Chem., Int. Ed.*, 2023, **62**, e202216089.
22 Y. Liu, S. Liu, X. Xie, Z. Li, P. Wang, B. Lu, S. Liang, Y. Tang and J. Zhou, *InfoMat*, 2023, **5**, e12374.
23 F. Wang, O. Borodin, T. Gao, X. Fan, W. Sun, F. Han, A. Faraone, J. A. Dura, K. Xu and C. Wang, *Nat. Mater.*, 2018, **17**, 543–549.
24 Z. Liu, Q. Yang, D. Wang, G. Liang, Y. Zhu, F. Mo, Z. Huang, X. Li, L. Ma and T. Tang, *Adv. Energy Mater.*, 2019, **9**, 1902473.
25 W. Pan, Y. Wang, X. Zhao, Y. Zhao, X. Liu, J. Xuan, H. Wang and D. Y. C. Leung, *Adv. Funct. Mater.*, 2021, **31**, 2008783.
26 C. Zhong, B. Liu, J. Ding, X. Liu, Y. Zhong, Y. Li, C. Sun, X. Han, Y. Deng and N. Zhao, *Nat. Energy*, 2020, **5**, 440–449.
27 D. Chao, C. Ye, F. Xie, W. Zhou, Q. Zhang, Q. Gu, K. Davey, L. Gu and S. Z. Qiao, *Adv. Mater.*, 2020, **32**, 2001894.
28 Y.-f Cui, Y.-h Zhu, J.-y Du, Y.-l Zhang, K. Li, W.-q Liu, G. Huang and X.-b Zhang, *Joule*, 2022, **6**, 1617–1631.
29 W. Shang, W. Yu, Y. Liu, R. Li, Y. Dai, C. Cheng, P. Tan and M. Ni, *Energy Storage Mater.*, 2020, **31**, 44–57.
30 J. Wang, L. Zhang, C. Zhang and J. Zhang, *J. Power Sources*, 2001, **102**, 139–143.
31 Z. Zhao, X. Fan, J. Ding, W. Hu, C. Zhong and J. Lu, *ACS Energy Lett.*, 2019, **4**, 2259–2270.
32 Y. Song, P. Ruan, C. Mao, Y. Chang, L. Wang, L. Dai, P. Zhou, B. Lu, J. Zhou and Z. He, *Nano-Micro Lett.*, 2022, **14**, 218.
33 C. Bai, F. Cai, L. Wang, S. Guo, X. Liu and Z. Yuan, *Nano Res.*, 2018, **11**, 3548–3554.
34 K. Amine, H. Yasuda and M. Yamachi, *Electrochem. Solid-State Lett.*, 2000, **3**, 178.
35 H. Lim, A. Lackner and R. Knechtli, *J. Electrochem. Soc.*, 1977, **124**, 1154.
36 C. Yang, X. Ji, X. Fan, T. Gao, L. Suo, F. Wang, W. Sun, J. Chen, L. Chen and F. Han, *Adv. Mater.*, 2017, **29**, 1701972.
37 H. Y. Shi, Y. Song, Z. Qin, C. Li, D. Guo, X. X. Liu and X. Sun, *Angew. Chem., Int. Ed.*, 2019, **58**, 16057–16061.
38 H. Pan, Y. Shao, P. Yan, Y. Cheng, K. S. Han, Z. Nie, C. Wang, J. Yang, X. Li and P. Bhattacharya, *Nat. Energy*, 2016, **1**, 1–7.
39 P. Senguttuvan, S. D. Han, S. Kim, A. L. Lipson, S. Tepavcevic, T. T. Fister, I. D. Bloom, A. K. Burrell and C. S. Johnson, *Adv. Energy Mater.*, 2016, **6**, 1600826.
40 W. Zhang, C. Zuo, C. Tang, W. Tang, B. Lan, X. Fu, S. Dong and P. Luo, *Energy Technol.*, 2021, **9**, 2000789.
41 Y. Lyu, X. Wu, K. Wang, Z. Feng, T. Cheng, Y. Liu, M. Wang, R. Chen, L. Xu and J. Zhou, *Adv. Energy Mater.*, 2021, **11**, 2000982.
42 G. Zampardi and F. La Mantia, *Curr. Opin. Electrochem.*, 2020, **21**, 84–92.
43 A. K. Padhi, K. S. Nanjundaswamy and J. B. Goodenough, *J. Electrochem. Soc.*, 1997, **144**, 1188.
44 T.-F. Yi, C.-L. Hao, C.-B. Yue, R.-S. Zhu and J. Shu, *Synth. Met.*, 2009, **159**, 1255–1260.
45 R. Santhanam and B. Rambabu, *J. Power Sources*, 2010, **195**, 5442–5451.
46 L. Chen, X. Fan, E. Hu, X. Ji, J. Chen, S. Hou, T. Deng, J. Li, D. Su and X. Yang, *Chem*, 2019, **5**, 896–912.
47 J. Hao, J. Long, B. Li, X. Li, S. Zhang, F. Yang, X. Zeng, Z. Yang, W. K. Pang and Z. Guo, *Adv. Funct. Mater.*, 2019, **29**, 1903605.
48 W. Xiong, D. Yang, T. K. Hoang, M. Ahmed, J. Zhi, X. Qiu and P. Chen, *Energy Storage Mater.*, 2018, **15**, 131–138.
49 Y. Zhang and M. Muhammed, *Hydrometallurgy*, 2001, **60**, 215–236.
50 K.-W. Nam, W.-S. Yoon, H. Shin, K. Y. Chung, S. Choi and X.-Q. Yang, *J. Power Sources*, 2009, **192**, 652–659.
51 T. Liu, A. Dai, J. Lu, Y. Yuan, Y. Xiao, L. Yu, M. Li, J. Gim, L. Ma and J. Liu, *Nat. Commun.*, 2019, **10**, 1–11.
52 X. Tang, J. Zhou, M. Bai, W. Wu, S. Li and Y. Ma, *J. Mater. Chem. A*, 2019, **7**, 13364–13371.
53 L. Ma, N. Li, C. Long, B. Dong, D. Fang, Z. Liu, Y. Zhao, X. Li, J. Fan and S. Chen, *Adv. Funct. Mater.*, 2019, **29**, 1906142.
54 J. Hao, X. Li, S. Zhang, F. Yang, X. Zeng, S. Zhang, G. Bo, C. Wang and Z. Guo, *Adv. Funct. Mater.*, 2020, **30**, 2001263.
55 Y. Luo, *In situ and ex situ studies of materials with relevance to electrochemical energy storage and energy generation*, Case Western Reserve University, 2002.
56 T. Gao, Y. Sun, L. Gong, C. Ma, J. Wang and L. Su, *J. Electrochem. Soc.*, 2020, **167**, 020552.
57 N. Zhang, Y. Dong, M. Jia, X. Bian, Y. Wang, M. Qiu, J. Xu, Y. Liu, L. Jiao and F. Cheng, *ACS Energy Lett.*, 2018, **3**, 1366–1372.
58 F. Wan, Y. Zhang, L. Zhang, D. Liu, C. Wang, L. Song, Z. Niu and J. Chen, *Angew. Chem., Int. Ed.*, 2019, **58**, 7062–7067.
59 I. A. Rodríguez-Pérez, L. Zhang, J. M. Wrogemann, D. M. Driscoll, M. L. Sushko, K. S. Han, J. L. Fulton, M. H. Engelhard, M. Balasubramanian and V. V. Viswanathan, *Adv. Energy Mater.*, 2020, **10**, 2001256.
60 L. Zhang, L. Chen, X. Zhou and Z. Liu, *Adv. Energy Mater.*, 2015, **5**, 1400930.
61 N. Zhang, F. Cheng, Y. Liu, Q. Zhao, K. Lei, C. Chen, X. Liu and J. Chen, *J. Am. Chem. Soc.*, 2016, **138**, 12894–12901.
62 M. Gong, Y. Li, H. Zhang, B. Zhang, W. Zhou, J. Feng, H. Wang, Y. Liang, Z. Fan and J. Liu, *Energy Environ. Sci.*, 2014, **7**, 2025–2032.
63 X. Xu, S. Deng, H. Wang, J. Liu and H. Yan, *Nano-Micro Lett.*, 2017, **9**, 1–19.
64 H. J. Lee, Z. Brown, Y. Zhao, J. Fawdon, W. Song, J. H. Lee, J. Ihli and M. Pasta, *Chem. Mater.*, 2021, **33**, 1238–1248.
65 L. Chen, X. Fan, E. Hu, X. Ji, J. Chen, S. Hou, T. Deng, J. Li, D. Su and X. Yang, *Chem*, 2019, **5**, 896–912.
66 Z. Chang, Y. Qiao, H. Yang, H. Deng, X. Zhu, P. He and H. Zhou, *Energy Environ. Sci.*, 2020, **13**, 4122–4131.
67 M. Hu, Y. Tian, L. Su, J. Wei and Z. Zhou, *ACS Appl. Mater. Interfaces*, 2013, **5**, 12185–12189.

